Received: 3 July 2023 | Revised: 29 August 2023 | Accepted: 4 September 2023

DOI: 10.1002/pen.26495

RESEARCH ARTICLE

POLYMER ENGINEERING AND SCIENCE WILEY

# Interrelationships between process parameters, cross-sectional geometry, fracture behavior, and mechanical properties in material extrusion additive manufacturing

**Ahmed O. Adisa** | **Austin R. Colon** | **David O. Kazmer** | **Amy M. Peterson**

Department of Plastics Engineering, University of Massachusetts Lowell, Lowell, Massachusetts, USA

**Correspondence**
Amy M. Peterson, University of Massachusetts Lowell, Department of Plastics Engineering, Lowell, MA, USA.
Email: amy_peterson@uml.edu

**Funding information**
Division of Civil, Mechanical and Manufacturing Innovation, Grant/Award Number: 1914651

## Abstract

Additive manufacturing offers reduced lead time between design and manufacturing. Fused filament fabrication, the most common form of material extrusion additive manufacturing, enables the production of custom-made parts with complex geometry. Despite the numerous advantages of additive manufacturing, reliability, reproducibility, and achievement of isotropic bulk properties in part remains challenging. We investigated the tensile behavior of a model polycarbonate system to explore what leads to different tensile properties, including sources of ductile versus brittle fracture. We utilized a one factor at a time (OFAT) design of experiments (DOE), printed single road-width boxes, and performed tensile tests on specimens from these boxes. Additionally, we characterized the cross-sections of parts printed under different conditions and their subsequent fracture behavior. The results demonstrate that isotropic bulk properties are achievable by printing at high speeds, and provide mechanisms to explain why.

## Highlights

- Printing at high speeds leads to improved mechanical properties.
- Printed samples undergo a mix of ductile and brittle failure.
- Jagged fracture path is associated with superior adhesion.
- High layer times lead to worse interfacial bonding.

KEYWORDS

additive manufacturing, fracture, mechanical properties, microscopy, voids

## 1 | INTRODUCTION

Material extrusion is the most widely used form of additive manufacturing (AM), with desktop scale thermally-driven fused filament fabrication (FFF) being the most common form of material extrusion additive manufacturing. FFF enables the production of custom-made parts with complex geometry and offers reduced lead times. Despite FFF's popularity, parts fabricated with FFF tend to be weaker and more brittle than those fabricated with traditional thermoplastic formative manufacturing (e.g., injection molding, extrusion) or other forms of thermoplastic AM (e.g., powder bed fusion/selective laser sintering).[1–3] Worse properties may be caused by poor interlayer welding,[4,5] the presence

of voids,[6,7] extrudate shape,[8,9] compositional variation across the extruded road,[10] or a combination of factors.

Poor interlayer strength (i.e., z-strength) in FFF structures is a key limitation to broader adoption of FFF, so its causes have been widely investigated. Sources of poor interlayer strength can broadly be described as rapid cooling, polymer conformation, and surface topography, each of which is described in more detail below. Rapid cooling of the extrudate was the first cause of poor z-strength that was identified.[3,11] Experimental studies have shown that the extrudate cools below the glass transition temperature ($T_g$) within a few seconds of exiting the nozzle.[12–15] Seppala and Migler observed a cooling rate of 100°C/s.[13] This rapid cooling limits both the extent of neck growth and polymer welding at the interface, thereby reducing the strength.[4] McIlroy and Olmsted observed that there is insufficient time for entangled polymer chains to relax and randomize during cooling,[10] which leads to reduction in strength at the weld interface due to the presence of residual alignment of the polymer chain.[5,16] Allum et al. reported that the surface topography of FFF parts, with the characteristic stacked layers of extrudate, leads to stress concentration in the notches that reduces the strength and fracture toughness even when conditions are appropriate for full welding.[8] Kundurthi et al. also showed that the stress concentration factor, which is due to the geometry of stacked layers, reduces the effective z-strength.[9]

Mechanical properties of FFF samples are known to depend on processing parameters such as infill density, print speed, build orientation, raster orientation, extrusion temperature, and layer height.[17–22] Acrylonitrile butadiene styrene (ABS) printed at different print speeds showed similar stress–strain curves, but different strains to failure. Increasing print speed increased the strain to failure and elongation, while lower print speeds were associated with higher tensile strength. This behavior is attributed to improvements in the fracture resistance due to plastic deformation at the crack tip when printing at high speeds.[23] In acrylonitrile styrene acrylate (ASA), strain to failure was also found to increase with extrusion temperature.[24] Printing in the XZ build orientation led to better flexural and fatigue behavior in Polyamide 6 compared with printing in the XY orientation.[25] Layer height and extrusion temperature were found to be essential in determining the mechanical response in printed polycarbonate, showing anti-synergistic effects.[26]

The fracture path within printed structures tends to follow the interface between layers due to the previously discussed issues. However, this is not always the case, and higher part strength can result when the fracture crosses multiple part interfaces. For example, fracture across multiple layers was observed by Ryder et al. for a stainless steel-filled ABS.[27] Additionally, in the work of Pourali and Peterson in which a semicrystalline hot melt adhesive was printed, the fracture path with respect to layer location could not be determined due to difficulty in identifying the location of the interface because of the excellent part consolidation.[18] Similarly, Zhang et al. reported no obvious interfacial fracture in tensile testing of polylactic acid (PLA).[28] Kazmer and Colon also observed fractures crossing multiple layer interfaces and near isotropic part strength with a hybrid injection printing technique.[29]

In this work, we investigate the tensile behavior of a model polycarbonate system to explore what leads to different tensile properties. We use a one factor at a time (OFAT) design of experiments (DOE), print single road width boxes, and perform tensile test on specimens from these boxes. OFAT, which has been used in several other studies,[30–33] is an efficient and effective approach for identifying the main and second order effects of individual variables, requiring fewer experiments than many other DOEs. Additionally, we characterize the cross-sections of parts printed under different conditions. Then, we categorize the fracture behavior and relate this behavior to print conditions and cross-sectional geometry to understand the range of fracture behaviors we can achieve and what leads to these behaviors. To the authors' knowledge, this is the first instance that holistically examines part geometry, fracture surface, fracture path, and stress–strain curve in combination to explore the causes of reduction in tensile properties in FFF parts.

## 2 | MATERIALS AND METHODS

### 2.1 | Materials

Transparent premium polycarbonate filament (Raise3D) with a diameter of 1.75 mm was used in this study. The $T_g$ was measured to be 112.7°C from differential scanning calorimetry (DSC, Figure S1). Before use, the filament was dried at 75°C for 6 h and the filament spool was kept in the dryer (PrintDry Filament Dryer PRO) and connected to the printer through the filament exit port to minimize moisture absorption while printing.

### 2.2 | Material extrusion

Single wall hollow boxes (60 × 60 × 60 mm) were printed on a Creality Ender 5 Pro Printer with a custom bronze hot end (i.Materialise), which was machined to specification, and 0.4 mm internal diameter brass nozzle (McMaster-Carr). The printer used a Micro Swiss direct extrusion system to deliver the filament to the hot end. The set-up incorporates a 5 kg load cell from Sparkfun,

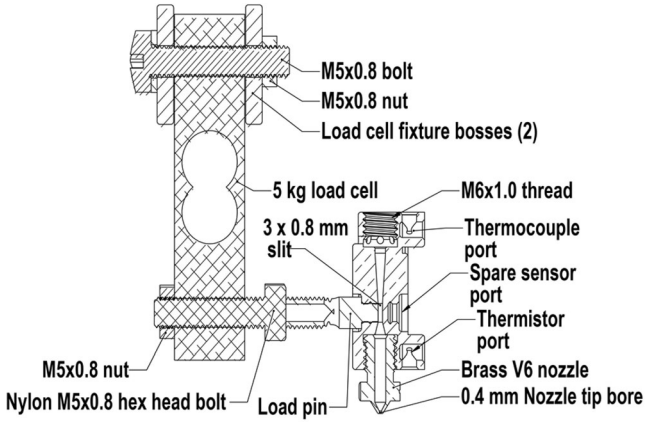


**FIGURE 1** Cross-sectional view of the hot end system.

while factory heat break and heat sink were used. Figure 1 shows the hot end's cross-sectional geometry.

Printing was performed in a residential apartment during the COVID-19 pandemic, so ambient temperature ranged from 20°C to 28°C. G-code was written with MATLAB for printing of the hollow boxes. Print parameters are listed in Table 1. Extrusion temperatures were selected based on the filament's specifications, print speeds were selected to reflect what is commonly encountered in practice, and layer times were chosen across a wide range. Layer time refers to the time needed to complete printing a single layer, return to a given XY position for the next layer, and dwell to purposefully maintain the specified timing between deposition of subsequent layers. A layer height of 0.2 mm, target layer width of 0.628 mm, and bed temperature of 90°C were maintained throughout the experiments. Comparison of conditions 1, 2, and 3 allows for direct assessment of the effect of extruder temperature. Comparison of conditions 1, 4, and 5 allows for investigation of the effect of print speed; however, it should be noted that layer time also changes with print speed. Conditions 4 and 6 have similar layer times and different print speeds, so their comparison is preferable to 1, 4, and 5 for print speed independent of layer time. The effect of layer time, independent of print speed, can be assessed through comparison of conditions 1, 6, and 7.

## 2.3 | Tensile testing

For each condition, ASTM D638 Type V tensile bars were die cut from the printed boxes such that the layers were perpendicular to the loading direction. Tensile testing was performed on the Type V tensile bars using an Instron 5966 Universal Testing machine with a 10 kN load cell. Testing was conducted in accordance with ASTM D638-14 using a crosshead speed of 1 mm $min^{-1}$ (strain rate of 0.1 mm (mm $min)^{-1}$). An average of 13 tests with failure within the gage region were obtained per print condition.

**TABLE 1** Print parameters for single road hollow box.

| Condition | Extrusion temperature (°C) | Print velocity (mm/s) | Layer time (s) |
|---|---|---|---|
| 1 (base) | 260 | 30 | 8.09 |
| 2 | 240 | 30 | 8.09 |
| 3 | 280 | 30 | 8.09 |
| 4 | 260 | 12.5 | 23.54 |
| 5 | 260 | 90 | 3.49 |
| 6 | 260 | 30 | 20.09 |
| 7 | 260 | 30 | 60.35 |

## 2.4 | Optical microscopy

Optical microscopy was performed using a Leica MC170 HD to evaluate the dimensions of printed roads and the fracture path from tensile testing. To evaluate the dimensions of printed road, specimens were fractured along the *Z*-axis (perpendicular to the printing plane) before imaging. The road width, weld width, road height, and cross-sectional area were measured away from the edges of the box. Contact ratio was determined as the ratio of the weld width to the adjacent road width. Twenty measurements of each parameter were taken per print condition.

## 2.5 | Scanning electron microscopy

A JEOL JSM 6390 was used to perform scanning electron microscopy (SEM) after gold sputtering samples with a Denton Vacuum Desk IV Sputter coater. Surfaces were imaged to examine defects and to perform fractography.

## 2.6 | Statistics

One-way analysis of variance (ANOVA) was used to assess statistical significance. A 95% confidence interval ($p < 0.05$) was used for all analysis.

# 3 | RESULTS AND DISCUSSION

## 3.1 | Cross-sectional analysis

Road width, road height, weld width, contact ratio, and road cross-sectional area in single road width walls were

assessed for each condition. Figure 2 shows weld width, road width, road height, and contact ratios as a function of layer time, print speed, and extrusion temperature. In general, we do not expect road height to be affected by print conditions due to the rapid cooling inherent to FFF, and, indeed, we do not see road height changing with any of these process parameters. The measured road height values conform to Equation (1)[34]:

$$H = g \text{ when } g < D\sqrt{\frac{U}{V}}, \tag{1}$$

where $H$ is the measured layer height, $g$ is the specified gap height, $D$ is nozzle diameter, $U$ is extrusion velocity in nozzle, and $V$ is print velocity. Other road quantities show dependence on layer time, print speed, and/or extrusion temperature, which is discussed in more detail below. In all cases, weld width and road width show similar trends. No effect of print speed independent of layer time was observed.

The effect of layer time is shown in Figure 2A, which compares conditions 1, 6, and 7. For samples printed at an intermediate layer time of 20 s, we observe that the road width was significantly larger compared with prints with 8 and 60 s layer time, which had similar road width values. Similar to road width, the contact ratio for a layer time 20 s was highest, and statistically differs from those at 8 and 60 s layer time, which were both similar. This observed optimum value of layer time at 20 s to achieve the maximum contact ratio is curious, although we note that the difference between minimum and maximum contact ratio is small at 4%.

Conditions 1, 4, and 5 are compared in Figure 2B to assess the effect of print speed. Road width shows a strong decrease with increasing print speed. As shown in Figure 3, increasing the print speed to 90 mm/s led to a road width smaller than the nozzle diameter, both of which are much lower than the target road width of 0.628 mm. As the print speed increases, so does the volumetric flow rate. The expected volumetric flow rates

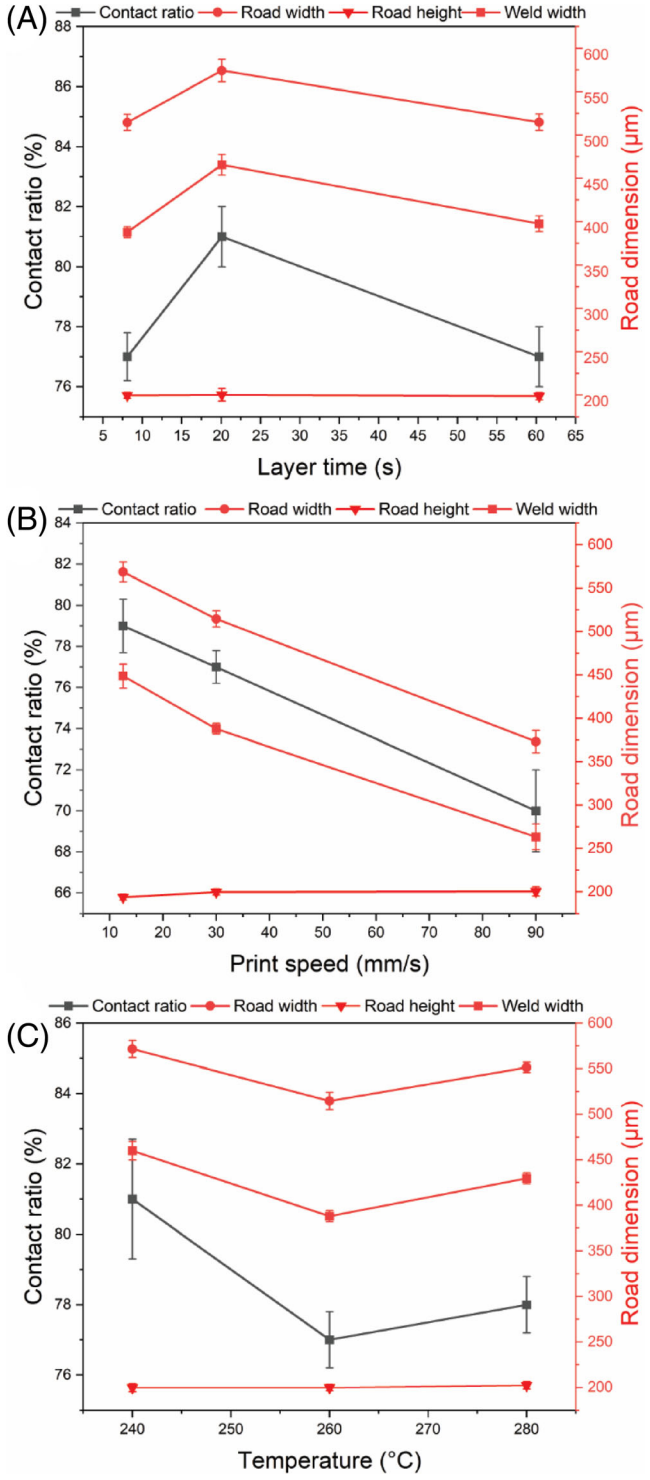


FIGURE 2 Contact ratio, road width, weld width, and road height as a function of (A) layer time, (B) print speed, and (C) extrusion temperature. Error bars indicate 95% confidence interval.

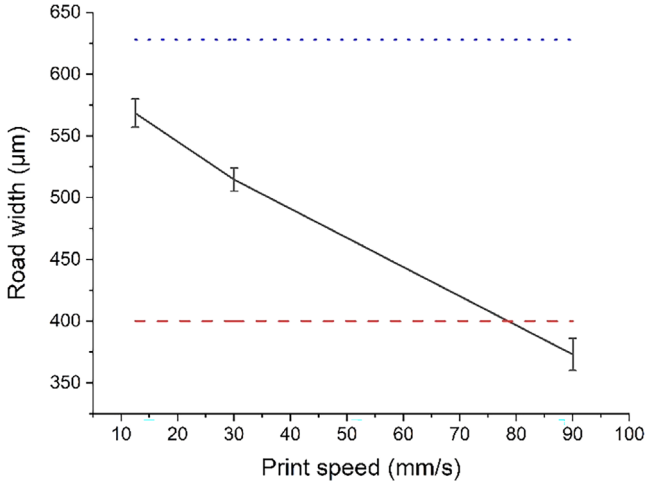


FIGURE 3 Road width as a function of print speed. Error bars indicate 95% confidence interval. The dashed lines represent the nozzle diameter, and the dotted line indicates the target width.

at print speeds of 12.5, 30, and 90 mm/s are 1.57, 3.77, and 11.31 $mm^3/s$, respectively. However, leaking from one of the ports was observed, which would lower actual volumetric flow rates and explain the below target road widths. Additionally, in a similar hot end, Kazmer et al. found that flow rates above 5 $mm^3/s$ exceed the hot end melt capacity, leading to lower extrudate temperatures and higher melt viscosities.[35] At high target volumetric flow rates, achieved volumetric flow rates may be lower than the target due to limitations in the hot end melt capacity and increased fluid pressure.

The maximum contact ratio of 79% occurred at a print speed of 12.5 mm/s, while the smallest contact ratio of 70% was associated with a print speed of 90 mm/s. Contact ratio decreases with increasing print speed, which is consistent with the findings of Abbot et al.[36] One probable cause is the insufficient melting of the filament in the hot end before extrusion due to the high print speed, which led to a lower extrudate temperature and higher viscosity, thereby limiting its spread. As we see from the micrographs in Figure 4, the extrudate at high print speeds has a more circular cross-section, while the extrudate at lower print speeds has a more oval-shaped cross-section. Similar to the findings of Coogan and Kazmer, print speed showed the most significant contribution to variation of the weld width.[37] Weld width decreased with increasing print speed, with samples printed at 90 mm/s having the lowest weld width, as shown in Figure 2B.

The effect of extrusion temperature is shown in Figure 2C. No clear trend was observed in road width or weld width as a function of extrusion temperature. Ai et al. reported no significant effect of temperature on the road width.[38] Coogan and Kazmer reported a slight increase in weld width with increasing temperature.[4] The lowest extrusion temperature led to the highest contact ratio of 81%, while extrusion temperatures of 260°C and 280°C have contact ratios of 77% and 78%, respectively. Due to the low viscosity at elevated temperatures, an increase in temperature should give a higher contact ratio.[39] However, the high melt pressure associated with the low melt temperature may have forced extrudate spreading. Die swell will be greater at low extrusion temperatures due to increased melt viscosities, which could lead to an increase in cross-sectional area and, consequently, contact ratio.

Road cross-sectional areas decreased with increasing print speed. Based on conservation of mass, the expected road cross-sectional area is 0.1256 $mm^2$. All cross-sectional areas are below this value. Low cross-sectional areas could be caused by under-extrusion; however, since lower than expected cross-sectional areas are observed even for low volumetric flow rates, this is not the only contributed factor. Roads may also be drawn down to some extent as they are printed, which could occur under all print conditions. Further exploration of this phenomenon is an important area of future research. Under-extrusion also contributes and would increase with increasing print speed as shown in Figure 5B. As was previously discussed in the context of road width, insufficient melt capacity likely limits the amount of extrudate at 90 mm/s. Levinskas also reported that under-extrusion increases with increasing flow rate, consistent with our results.[40]

Road cross-sectional area did not change when layer time increased from 8.09 to 20 s, but showed a significant decrease upon further increasing layer time to 60 s as shown in Figure 5A. This decrease in road cross-sectional area could be due to thermal stresses generated as a result of the higher temperature gradient in samples printed with longer layer times.[41] When printing at short layer times, the preceding layer has less time to cool, so it does not cool as much and will be heated to a higher temperature by the subsequent layer. Extrusion temperature did not affect the cross-sectional area in a statistically significant manner.

## 3.2 | Tensile properties

Tensile properties of printed and compression molded samples are summarized in Table 2. On average, printed samples showed lower tensile strength than compression

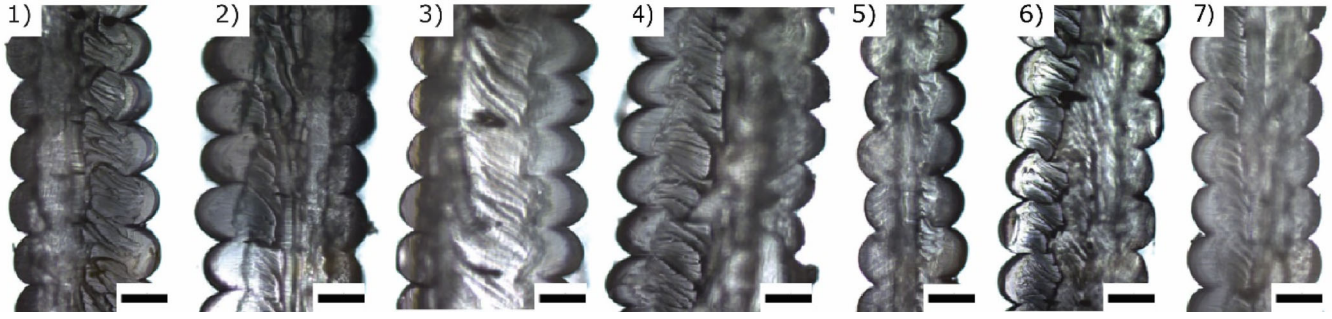


FIGURE 4 Representative cross-sections of printed samples for print conditions 1–7. Scale bars represent 200 μm.

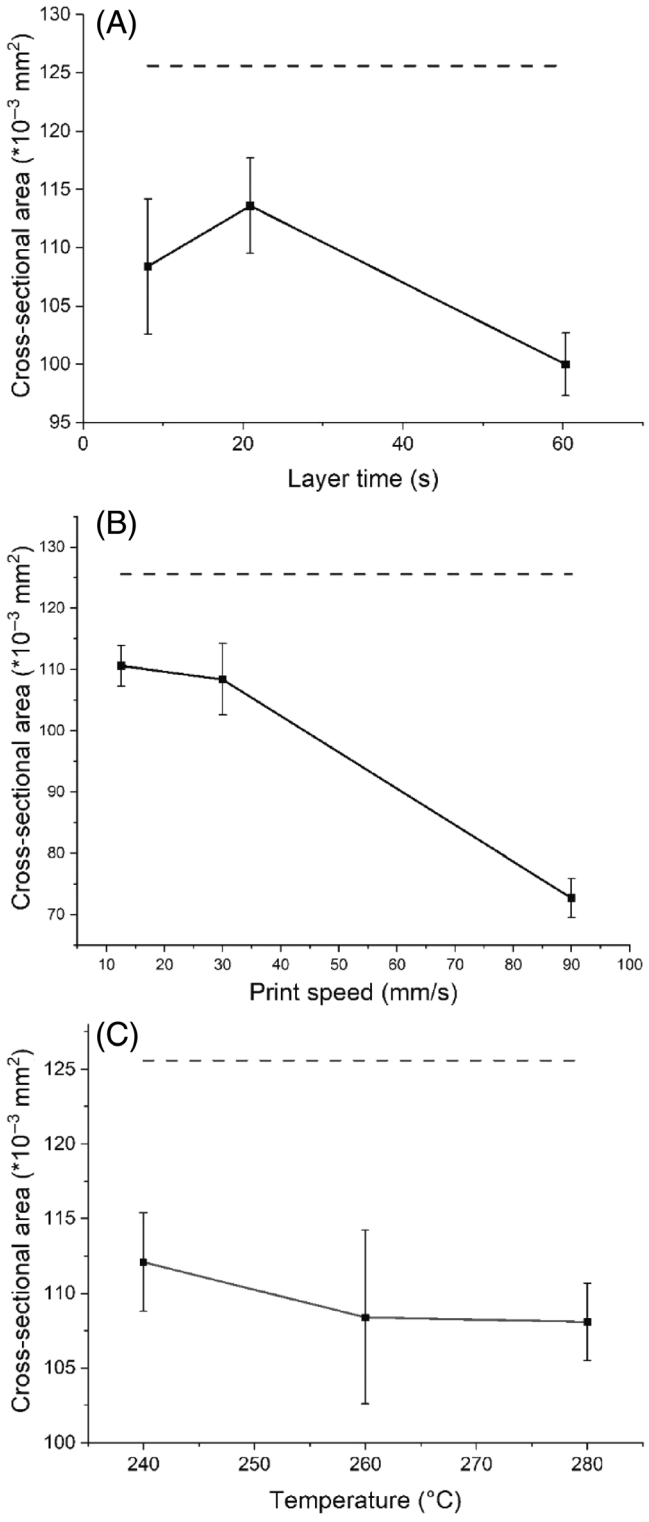


**FIGURE 5** Cross-sectional area as a function of (A) layer time, (B) print speed, and (C) temperature. Dashed lines represent the expected cross-sectional area based on conservation of mass. Error bars indicate 95% confidence interval.

molded ones (41.3 ± 3.8 MPa vs. 59.7 ± 2.1 MPa). Excluding print conditions 3 and 5, printed samples have Young's moduli that are similar to the compression molded samples. The compression molded sample's Young's modulus of 1749 ± 166 MPa is lower than a literature value for PC (2236 ± 2 MPa),[21] while its tensile strength is within range (53.0 ± 5.8 MPa).[42] The PC used in this work also has a lower $T_g$ than typical PC grades (113°C vs. 140°C–149°C).[38,43–45] These variations in $T_g$ and Young's modulus are likely due to differences in material composition.

**TABLE 2** Tensile properties for printed and compression molded samples.

| Condition | Tensile strength (MPa) | Young's modulus (MPa) |
|---|---|---|
| 1 (base) | 37.7 ± 7.9 | 1870 ± 111 |
| 2 | 40.1 ± 6.2 | 1872 ± 83 |
| 3 | 41.4 ± 8.6 | 2055 ± 77 |
| 4 | 33.2 ± 4.7 | 1837 ± 82 |
| 5 | 59.7 ± 14.8 | 2284 ± 272 |
| 6 | 42.7 ± 3.5 | 1892 ± 62 |
| 7 | 30.1 ± 8.1 | 1906 ± 143 |
| Compression molded | 59.7 ± 2.1 | 1749 ± 166 |

*Note*: Averages and 95% confidence intervals are reported.

The effect of layer time is assessed by comparing condition 1, 6, and 7 as shown in Figure 6A. Young's modulus is independent of layer time, which is consistent with it being a measure of the material's stiffness in the elastic regime. Tensile strength increased, but not at a statistically significant level, when layer time increased from 8.09 to 20.09 s, but decreases significantly when layer time is further increased to 60.35 s. Increasing the layer time beyond 20 s allows the previous layer to cool so much that it reduces the amount of interlayer diffusion that can be achieved, leading to weaker bonds. Kuznetsov et al. found reduced strength with increasing layer time.[46] The tensile strengths of printed samples are lower than those of compression molded samples. Young's modulus values for printed and compression molded samples are generally in similar range, with some exceptions discussed below.

The effect of print speed is assessed by comparing conditions 1, 4, and 5, as shown in Figure 6B. Young's modulus remains unchanged when the print speed increases from 12.5 mm/s to 30 mm/s. However, upon further increase in print speed to 90 mm/s, the Young's modulus shows a significant increase. This increase in Young's modulus at the highest print speed can be ascribed to the improved interlayer welding, which occurs because there is less time for the previous layer to cool before deposition of a new layer.[33] Tensile strength

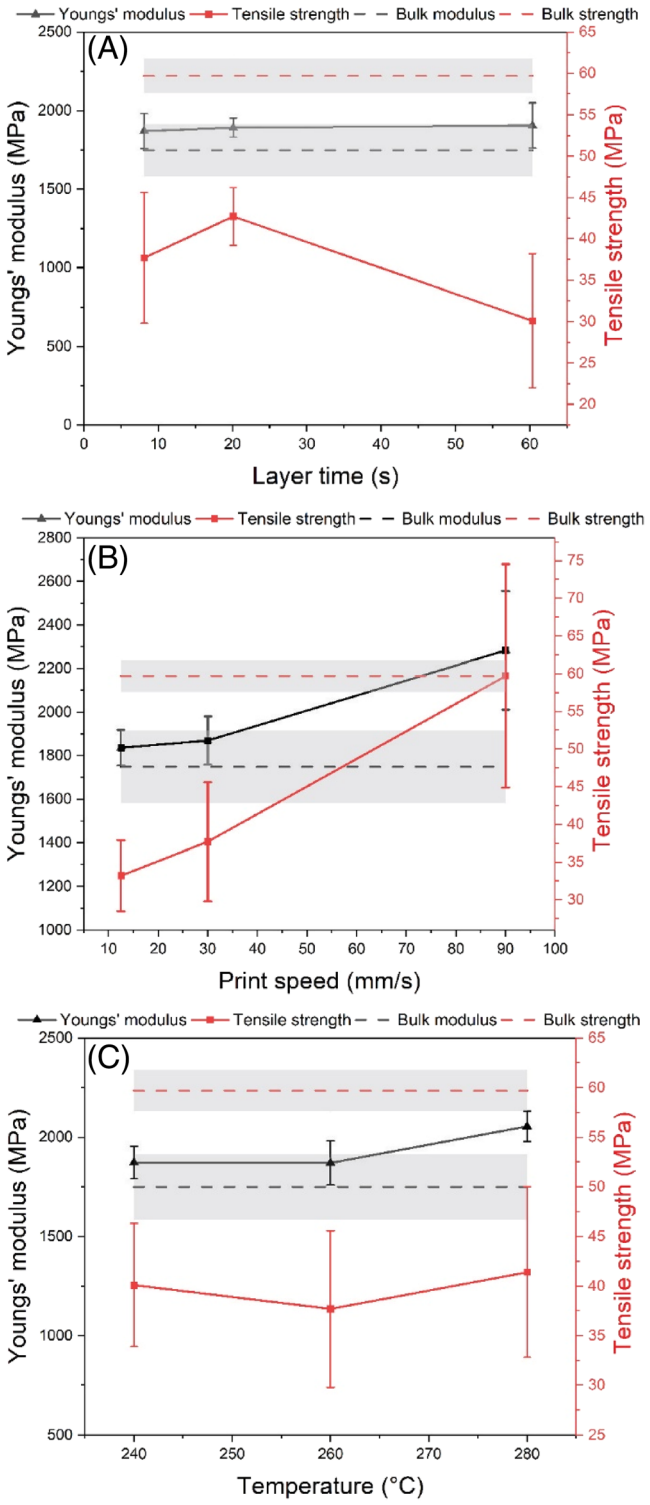


**FIGURE 6** Young's modulus and tensile strength versus (A) layer time, (B) print speed, and (C) extrusion temperature. Error bars indicate 95% confidence interval. The dashed lines indicate bulk properties (compression molded) and the grayed areas show the corresponding error.

remains unchanged when the print speed increases from 12.5 to 30 mm/s and shows a significant increase upon further increase to 90 mm/s. These results are consistent with the findings of Coogan et al., who reported an increase in bond strength with increasing print speed.[37] However, these results differ from the findings of Abbot et al., who observed a decrease in tensile strength upon increase in print speed.[36] The lack of consensus indicates that other related parameters (e.g., layer time) may confound this analysis.

The effect of extrusion temperature is assessed by comparing condition 1, 2, and 3, as shown in Figure 6C. Tensile strength shows no clear trend with increasing extrusion temperature, which differs from the generally expected and observed trend of increasing bond strength with increased extrusion temperature.[4,8,18,37,47] One possible reason for this deviation from expected behavior is that the contact ratio for an extrusion temperature of 240°C is 3%–4% higher than for 260°C and 280°C. Young's modulus stays in the same range when extrusion temperature increases from 240°C to 260°C and then increases upon increasing the extrusion temperature to 280°C. The increase between 260°C and 280°C could be due to improved interlayer adhesion at the interface and diffusion of the polymer chains since they stay above $T_g$ for more time.

Obtaining accurate measurements of part and weld dimensions is critical to achieving high-quality mechanical data. In this work, we use the weld thickness from optical microscopy in the area for calculating tensile strength. However, a simpler option is to use calipers to determine thickness. For most print conditions, the difference is not substantial (see comparative data in Table S1). However, print condition 5 showed a large difference. We observe that using the thickness obtained from the caliper measurement gives lower strength values than those obtained with the microscope obtained thickness ($41.0 \pm 9.32$ MPa vs. $59.7 \pm 14.79$ MPa). This difference is due to error introduced by the caliper measurement that overestimates the specimen thickness. We also observe that assuming full contact underestimates the actual tensile strength of the sample. ($41.8 \pm 10.35$ MPa vs. $59.7 \pm 14.79$ MPa). The large variance in the data for the tensile strength at the actual 70% contact ratio is a result of the use of mean values of the measured thickness and contact in our calculations. The tensile strength of this print condition is similar to the tensile strength of the compression molded sample ($59.7 \pm 14.79$ MPa vs. $59.7 \pm 2.1$ MPa), indicating complete welding and minimal stress-concentration. Given that the print speed of this condition was the highest, it implies that, at sufficiently high print speeds, complete welding is achievable during FFF. As we see from the micrograph in Figure 4, this print condition (5) has a more circular cross-section, which would have minimal stress concentration.[12]

Therefore, when sufficient welding is achieved, stress concentration becomes the main driver of the tensile strength.

While compression molded PC exhibited a large linear elastic regime, followed either by fracture or yielding and necking until failure, printed PC showed a wide range of tensile behaviors as seen in Figure 7. To explore this further, all stress–strain curves obtained from tensile testing were binned into seven shape-based categories to evaluate and understand the mechanical response. Figure 7 shows the representative plot of various curve categories and Table 3 shows the distribution of the curve categories in each print condition. Categories 1 and 2 represent failure in the strain-hardening region with category 1 exhibiting concavity in the strain-hardening region. Category 3 indicates failure in the strain-hardening region just after yielding, while category 4 shows failure in the elastic region. Category 5 shows failure after yielding before approaching the strain-hardening region. Category 6 is similar to category 4, except for its prominent toe region. Category 7 occurs only once, showing a slight strain softening before failure.

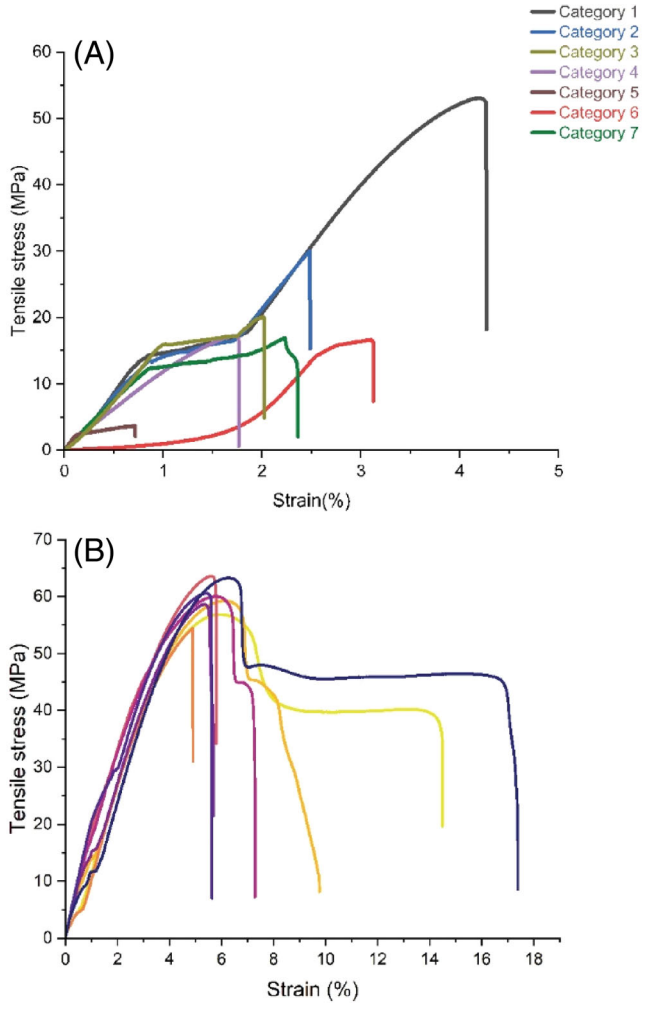


FIGURE 7 (A) Representative stress–strain curves for each category of printed sample. (B) Stress–strain curves for tensile testing of compression molded samples.

Categories 1 and 2 were the most common at 30.8% and 45.7%, respectively. Categories 2, 3, and 5 are earlier failures of category 1 since they trace the same path but failed at different regions of the curve. Category 4 follows a slightly different path, while category 6 deviated completely showing a prominent toe region.

Categories 1, 2, 3, 5, and 7 exhibited yielding, while categories 4 and 6 failed before yielding. All categories excluding category 7, have similar strain at yield and similar yield strength. Category 7 could not be statistically evaluated because it occurred once. The similarity in yield stress and the corresponding strain indicates that the curves trace a similar path up to the yield point, beyond which some samples exhibit more strain hardening than others.

The tensile properties of the various curve categories are summarized in Table 4. Comparing the tensile strength and Young's modulus in categories 1 and 5, we conclude that a high Young's modulus does not imply high tensile strength. As expected, curves that do not show yielding exhibit lower Young's moduli than those that yielded, with the exception of category 7 ($n = 1$). Young's modulus values are similar for categories 4 and 6 despite category 6's notable toe region.

## 3.3 | Fracture propagation analysis

Failure was categorized based on the fracture propagation path as shown in Figure 8. The fracture for category a spans across layers. In category b, the fracture propagates smoothly across the sample at a layer interface. Category c has a jagged fracture path, category d has a jagged fracture with an additional fracture path that does not propagate across the sample completely. Category e has a fracture path with an undetached strand at the edge, and category f has a bump along the fracture path. All failures are initiated at the interface, implying that the interface remains the weakest link.

SEM images of the fracture path categories in Figure 9 reveal that, contrary to the expectation of a pure brittle failure typical of samples printed in the z-direction as reported in literature,[38,48,49] we observe a mix of ductile and brittle failure. All micrographs except for Figure 9A show some form of ductile failure. Figure 9A, which shows brittle failure, exhibits voids and corresponds to curve category 4 that failed in the linear elastic region. Figure 9A is from print condition 7, which has the second highest occurrence of curve category 4 and

**TABLE 3** Curve categories distribution in each print condition.

| Print condition | Curve category (number of observations) | | | | | | | Total |
|---|---|---|---|---|---|---|---|---|
| | 1 | 2 | 3 | 4 | 5 | 6 | 7 | |
| 1 | 4 | 4 | 1 | 1 | 1 | 1 | 1 | 13 |
| 2 | 3 | 9 | | | | 2 | | 14 |
| 3 | 6 | 8 | | | 1 | | | 15 |
| 4 | | 8 | 1 | | | | | 9 |
| 5 | 8 | | | 4 | | 3 | | 15 |
| 6 | 6 | 8 | | | | | | 14 |
| 7 | 2 | 6 | 1 | 3 | 1 | 1 | | 14 |
| Total | 29 | 43 | 3 | 8 | 3 | 7 | 1 | 94 |

**TABLE 4** Tensile properties and 95% confidence interval for each curve category.

| Curve category | Tensile strength (MPa) | Young's modulus (MPa) |
|---|---|---|
| 1 | 59.4 ± 6.3 | 2151 ± 145 |
| 2 | 37.7 ± 2.7 | 1916 ± 49 |
| 3 | 24.0 ± 1.7 | 2023 ± 230 |
| 4 | 24.6 ± 11.0 | 1857 ± 133 |
| 5 | 15.0 ± 13.4 | 2034 ± 430 |
| 6 | 35.5 ± 12.6 | 1715 ± 256 |
| 7 | 21.7 | 1751 |
| Compression molded | 59.7 ± 2.1 | 1749 ± 166 |

the lowest tensile strength. The presence of voids reduces the tensile strength and Young's modulus considerably. Samples in Figure 9B–F begin with brittle failure and rapid fracture propagation, then experience ductile failure. This behavior is likely due to the curved extrudate cross-section shape, which creates areas of stress concentration at the edges.[50] The plastic deformation observed in Figure 9B–F, which fall into curve categories 1 and 2, is consistent with the strain hardening in these stress–strain curves.

Fracture path category a, which cuts across multiple interfaces, is due to the presence of voids as seen in Figure 9A. Voids between layers change the fracture path since voids offer the path of least resistance. As explained in the previous section, this corresponds to curves with failure in the elastic region. Voids were observed in print condition 7 with the highest layer time of 60 s, indicating that high layer times lead to worse interfacial bonding. The cooling associated with high layer times creates a thermal gradient such that there is a mismatch of the coefficient of thermal expansion of the previous layer and the layer being deposited above it, causing microscopic flaws at the interface.[41]

The frequency of occurrence for each fracture path in each print condition is presented in Table 5. Category c was the most prevalent fracture path, with 54% occurrence across all print conditions. The highest occurrence of fracture path category c was in print condition 5 and 6, with 67% and 86% occurrence, respectively. Print condition 5 and 6 had the highest tensile strength of 59.7 ± 14.8 MPa and 42.7 ± 3.5 MPa, respectively, so this jagged fracture path is correlated with superior adhesion.

We see from Figure 10 that certain fracture paths are prevalent in some curve categories. Category c fracture path is prevalent in curve categories 1 and 3, while fracture category b is prevalent in curve type 5. Curve category 7 only has fracture category e.

Curve category 1 has fracture path c occurring the most, followed by fracture path f. This curve category has the highest tensile strength and a high Young's modulus. Curve categories 2 and 4 have predominantly fracture path b and c. Although the SEM image of fracture path c, which occurs the highest in curve category 3 shows ductile fracture, curve category 3 does not undergo considerable strain hardening compared with curve categories 1 and 2. Curve category 5, which is dominated by fracture path b as shown in Figure 7, has the lowest tensile strength. This result is unexpected because fracture path category b was observed for the sample in Figure 6B, which exhibited ductile failure. We expect that the ductility, which is associated with strain-hardening, should give high tensile strength. However, curve category 5 gave the lowest tensile strength due to the small elastic regime for this curve category such that strain hardening cannot make up for the post-yield strain hardening. On the other hand, fracture category b has a high Young's modulus. It may be that not all fracture path b exhibits ductility since

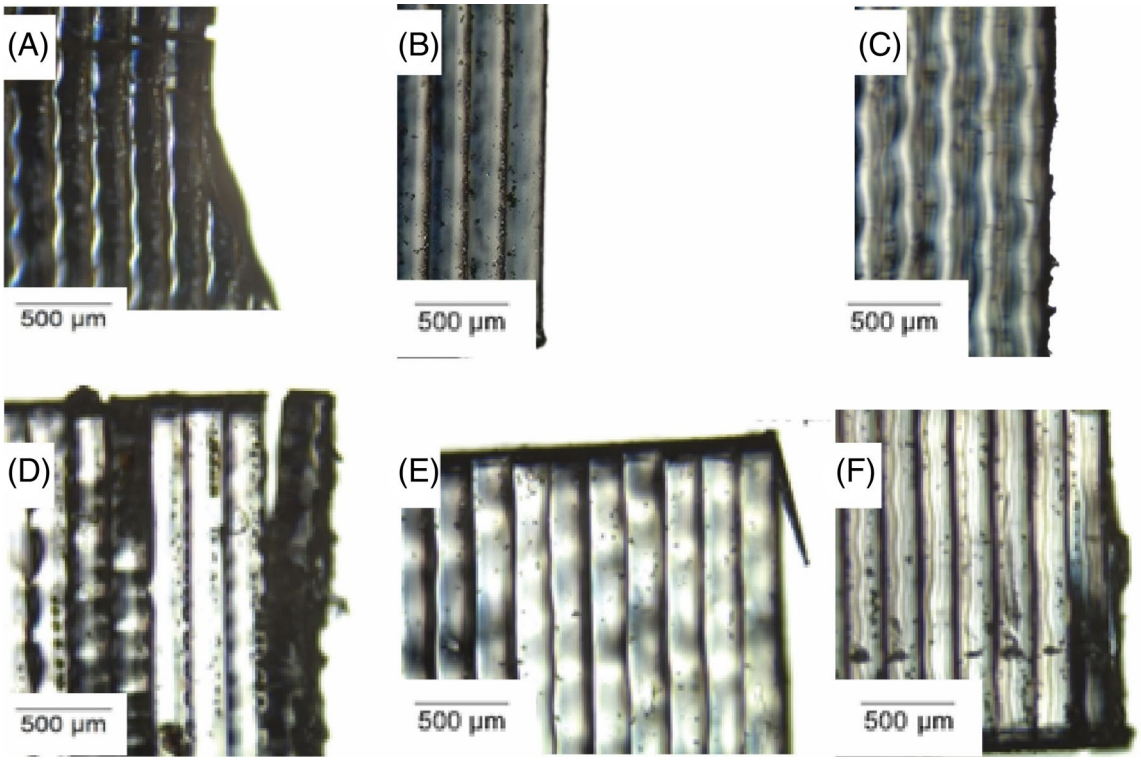


FIGURE 8 Representative optical micrographs of fracture path categories a–f.

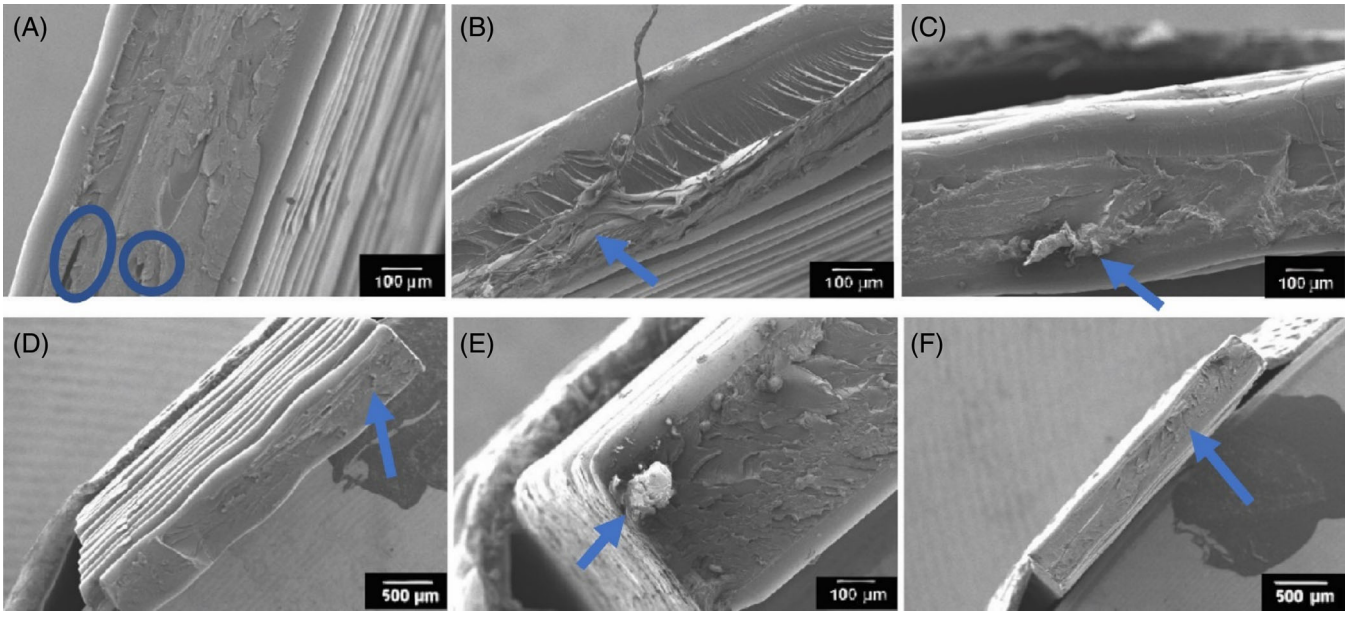


FIGURE 9 SEM of fracture surfaces associated with different types of fracture paths, as determined by optical microscopy. Print condition (PC) and curve category (CC) are indicated in parentheses for each micrograph. (A) Fracture across layers (PC 7, CC 4); (B) smooth fracture path (PC 1, CC 2); (C) jagged fracture path (PC 5, CC 1); (D) jagged fracture path with additional incomplete path (PC 2, CC 1); (E) fracture with an undetached strand at the edge—(PC 4, CC 2); (F) fracture with bump along path—(PC 5, CC 1). Plastic deformation is noted by blue arrows and voids are circled in.

we did not image all fracture path b surfaces. Curve category 6 is dominated by fracture path b and f, while curve category 7 ($n = 1$) falls under fracture path e.

In summary, the presence of a jagged fracture path is linked to high strain hardening, tensile strength, Young's modulus, and toughness (area under the stress–strain curve).

**TABLE 5** Prevalence of fracture path category in each print condition.

| | Fracture path category | | | | | | |
|---|---|---|---|---|---|---|---|
| **Print condition** | **a** | **b** | **c** | **d** | **e** | **f** | **Total** |
| 1 | 3 | - | 7 | 1 | 2 | | 13 |
| 2 | 2 | 3 | 6 | 1 | 1 | 1 | 14 |
| 3 | 1 | 3 | 8 | — | 1 | 2 | 15 |
| 4 | — | 2 | 3 | — | 1 | 3 | 9 |
| 5 | 1 | - | 10 | — | 4 | — | 15 |
| 6 | 1 | 1 | 12 | — | — | — | 14 |
| 7 | 2 | 4 | 5 | — | 1 | 2 | 14 |
| Total | 10 | 13 | 51 | 2 | 10 | 8 | 94 |

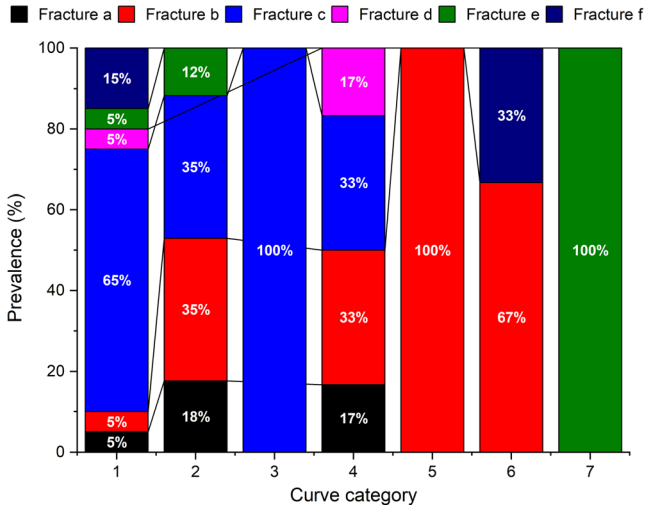


**FIGURE 10** Fracture path prevalence in various curve categories for 50 randomly selected printed samples.

This behavior is most prevalent in curve category 1 and print conditions 5 and 6. Smooth fracture paths dominate for curve category 5, which is associated with the lowest tensile strength, and is most commonly observed for print condition 7. These results indicate that samples printed at long layer times rarely undergo strain hardening and tend to fail with a smooth fracture path, while printing at high speeds encourages strain hardening, and is associated with fracture along a jagged fracture path.

## 4 | CONCLUSIONS

This study examines the effects of print speed, extrusion temperature, and layer time on tensile properties and extrudate (road) geometry. We also categorize the fracture behavior and relate this behavior to print conditions and cross-sectional geometry to understand the range of fracture behaviors we can achieve and what leads to these behaviors while relating the tensile properties to fracture behavior.

Tensile strength increases with increase in print speed, while extrusion temperature shows no clear trend. Young's modulus is unaffected by layer time, but shows dependence on extrusion temperature and print speed. We observe that a jagged fracture path, which occurs predominantly at high print speed and shorter layer times, is associated with high tensile strength and Young's modulus. On the other hand, we find the presence of voids on the fracture surface of samples printed with long layer times results in a reduction in strength. The presence of voids also leads to failure in the elastic region on the stress–strain curve. We see that the stress–strain curve is largely related to fracture path and that the curves with strain hardening region correlate to the jagged fracture path, which shows superior adhesion. Bulk strength was achieved in the $z$-direction at high print speed, indicating complete welding. Micrographs obtained from optical microscopy reveal that samples printed at high print speed have circular cross-sections, which are associated with lower stress concentration. Furthermore, SEM examination of fracture surfaces from high print speeds reveals a region of rapid crack propagation consistent with brittle failure, followed by a ductile failure region that is consistent with the strain hardening observed on the stress–strain curves. The rapid crack propagation is likely due to geometry-induced stress concentration.

These results demonstrate that printing at high speeds leads to improved tensile properties and provide mechanisms to explain why. When there is sufficient welding, the factor limiting the tensile strength is geometry-induced stress concentration. As a result, bulk properties can be achieved through print conditions that enable sufficient welding and produce a rounded groove tip geometry at the interface edges. However, bulk properties on a macro level (considering a solid printed structure with designed dimensions) will still be lower than expected if, as was observed in this work, cross-sectional areas are lower than expected. Hence, there is a need to achieve printing at high speeds, which minimizes stress concentration without the consequent reduction in cross-sectional area. Understanding the source of this difference and possible approaches to address this issue are important to advancing knowledge of the material extrusion additive manufacturing process and improving the reliability of structures. One possible way to address under-extrusion at high print speed would be implementation of a feedback control system.

The comprehensive approach adopted in this study adds valuable insights into the relationship between

geometry, fracture behavior, tensile properties, print parameters, and tensile strength. One limitation is the inability to obtain SEM images for all fracture surfaces, but we do see clear correlations between SEM, tensile testing results, and optical microscopy results, which suggests that optical microscopy in conjunction with the stress–strain curves can be used as a quick, low-cost screening method for fracture behavior in these types of additively manufactured structures.

## ACKNOWLEDGMENTS

This work is supported by the National Science Foundation (NSF) under GOALI Grant No. #1914651. The authors also acknowledge Stratasys, Ltd. as the University of Massachusetts Lowell team's GOALI partner.

## DATA AVAILABILITY STATEMENT

Micrographs and tensile testing results are available at DOI: 10.18126/p8jh-shxc.

## ORCID

*David O. Kazmer* https://orcid.org/0000-0002-1166-4043
*Amy M. Peterson* https://orcid.org/0000-0002-4612-0062

## REFERENCES

1. Dizon JRC, Espera AH, Chen Q, Advincula RC. Mechanical characterization of 3D-printed polymers. *Addit Manuf*. 2018;20:44-67. doi:10.1016/j.addma.2017.12.002
2. Peterson AM. Review of acrylonitrile butadiene styrene in fused filament fabrication: a plastics engineering-focused perspective. *Addit Manuf*. 2019;27:363-371. doi:10.1016/j.addma.2019.03.030
3. Ahn SH, Montero M, Odell D, Roundy S, Wright PK. Anisotropic material properties of fused deposition modeling ABS. *Rapid Prototyp J*. 2002;8(4):248-257. doi:10.1108/13552540210441166
4. Seppala JE, Hoon Han S, Hillgartner KE, Davis CS, Migler KB. Weld formation during material extrusion additive manufacturing. *Soft Matter*. 2017;13(38):6761-6769. doi:10.1039/c7sm00950j
5. McIlroy C, Olmsted PD. Disentanglement effects on welding behaviour of polymer melts during the fused-filament-fabrication method for additive manufacturing. *Polymer (Guildf)*. 2017;123:376-391. doi:10.1016/j.polymer.2017.06.051
6. Sun X, Mazur M, Cheng CT. A review of void reduction strategies in material extrusion-based additive manufacturing. *Addit Manuf*. 2023;67:103463. doi:10.1016/j.addma.2023.103463
7. Mazzanti V, Malagutti L, Mollica F. FDM 3D printing of polymers containing natural fillers: a review of their mechanical properties. *Polymers (Basel)*. 2019;11(7):1094.
8. Allum J, Gleadall A, Silberschmidt VV. Fracture of 3D-printed polymers: crucial role of filament-scale geometric features. *Eng Fract Mech*. 2020;224:106818. doi:10.1016/j.engfracmech.2019.106818
9. Kundurthi S, Tran F, Chen S, Mapkar J, Haq M. Bead geometry-induced stress concentration factors in material extrusion polymer additive manufacturing. *Rapid Prototyp J*. 2023;29:1438-1452. doi:10.1108/RPJ-11-2022-0404
10. Collinson DW, Kolluru PV, Von Windheim N, Brinson LC. Distribution of rubber particles in the weld zone of fused filament fabricated acrylonitrile butadiene styrene and the impact on weld strength. *Addit Manuf*. 2021;41:101964. doi:10.1016/j.addma.2021.101964
11. Bellini A, Güçeri S. Mechanical characterization of parts fabricated using fused deposition modeling. *Rapid Prototyp J*. 2003;9(4):252-264. doi:10.1108/13552540310489631
12. Kousiatza C, Karalekas D. In-situ monitoring of strain and temperature distributions during fused deposition modeling process. *Mater Des*. 2016;97:400-406. doi:10.1016/j.matdes.2016.02.099
13. Seppala JE, Migler KD. Infrared thermography of welding zones produced by polymer extrusion additive manufacturing. *Addit Manuf*. 2016;12:71-76. doi:10.1016/j.addma.2016.06.007
14. Sun Q, Rizvi GM, Bellehumeur CT, Gu P. Effect of processing conditions on the bonding quality of FDM polymer filaments. *Rapid Prototyp J*. 2008;14(2):72-80. doi:10.1108/13552540810862028
15. Dinwiddie RB, Kunc V, Lindal JM, et al. Infrared imaging of the polymer 3D-printing process. In: Ogasawara N, Ando H, Kobayashi C, Yamada H, eds. *Thermosense: Thermal Infrared Applications XXXVI*. Vol 9105. SPIE; 2014:910502. doi:10.1117/12.2053425
16. Costanzo A, Spotorno R, Candal MV, et al. Residual alignment and its effect on weld strength in material-extrusion 3D-printing of polylactic acid. *Addit Manuf*. 2020;36:101415. doi:10.1016/j.addma.2020.101415
17. Rodríguez-Panes A, Claver J, Camacho AM. The influence of manufacturing parameters on the mechanical behaviour of PLA and ABS pieces manufactured by FDM: a comparative analysis. *Materials*. 2018;11(8):1333. doi:10.3390/ma11081333
18. Pourali M, Peterson AM. Fused filament fabrication of void-free parts using low viscosity hot melt adhesives. *Addit Manuf*. 2021;46:102110. doi:10.1016/j.addma.2021.102110
19. Auffray L, Gouge PA, Hattali L. Design of experiment analysis on tensile properties of PLA samples produced by fused filament fabrication. *Int J Adv Manuf Technol*. 2022;118(11–12):4123-4137. doi:10.1007/s00170-021-08216-7
20. Pazhamannil RV, Nambhoodari VNJ, Govindhan P, Edacherian A. Property enhancement approaches of fused filament fabrication technology: a review. *Polym Eng Sci*. 2022;62(5):1356-1376. doi:10.1002/pen.25948
21. Fountas NA, Papantoniou I, Kechagias JD, Manolakos DE, Vaxevanidis NM. Modeling and optimization of flexural properties of FDM-processed PET-G specimens using RSM and GWO algorithm. *Eng Fail Anal*. 2022;138:106340. doi:10.1016/j.engfailanal.2022.106340
22. Kechagias J, Chaidas D. Fused filament fabrication parameter adjustments for sustainable 3D printing. *Mater Manuf Process*. 2023;38(8):933-940. doi:10.1080/10426914.2023.2176872
23. Rezaeian P, Ayatollahi MR, Nabavi-Kivi A, Mohammad Javad Razavi S. Effect of printing speed on tensile and fracture behavior of ABS specimens produced by fused deposition modeling. *Eng Fract Mech*. 2022;266:108393. doi:10.1016/j.engfracmech.2022.108393

24. El Magri A, Ouassil SE, Vaudreuil S. Effects of printing parameters on the tensile behavior of 3D-printed acrylonitrile styrene acrylate (ASA) material in Z direction. *Polym Eng Sci*. 2022; 62(3):848-860. doi:10.1002/pen.25891
25. Terekhina S, Tarasova T, Egorov S, Skornyakov I, Guillaumat L, Hattali ML. The effect of build orientation on both flexural quasi-static and fatigue behaviours of filament deposited PA6 polymer. *Int J Fatigue*. 2020;140:105825. doi:10.1016/j.ijfatigue.2020.105825
26. Vidakis N, Petousis M, Kechagias JD. A comprehensive investigation of the 3D printing parameters' effects on the mechanical response of polycarbonate in fused filament fabrication. *Prog Addit Manuf*. 2022;7(4):713-722. doi:10.1007/s40964-021-00258-3
27. Ryder MA, Lados DA, Iannacchione GS, Peterson AM. Fabrication and properties of novel polymer-metal composites using fused deposition modeling. *Compos Sci Technol*. 2018;158: 43-50. doi:10.1016/j.compscitech.2018.01.049
28. Zhang G, Wang Q, Ni Y, et al. A systematic investigation on the minimum tensile strengths and size effects of 3D printing polymers. *Polym Test*. 2023;117:107845. doi:10.1016/j.polymertesting.2022.107845
29. Kazmer DO, Colon A. Injection printing: additive molding via shell material extrusion and filling. *Addit Manuf*. 2020;36: 101469. doi:10.1016/j.addma.2020.101469
30. Wu WZ, Geng P, Zhao J, Zhang Y, Rosen DW, Zhang HB. Manufacture and thermal deformation analysis of semicrystalline polymer polyether ether ketone by 3D printing. *Mater Res Innov*. 2014;18:S5-12-S5-16. doi:10.1179/1432891714Z.000000000898
31. Yang C, Tian X, Li D, Cao Y, Zhao F, Shi C. Influence of thermal processing conditions in 3D printing on the crystallinity and mechanical properties of PEEK material. *J Mater Process Technol*. 2017;248:1-7. doi:10.1016/j.jmatprotec.2017.04.027
32. Wang P, Zou B, Xiao H, Ding S, Huang C. Effects of printing parameters of fused deposition modeling on mechanical properties, surface quality, and microstructure of PEEK. *J Mater Process Technol*. 2019;271:62-74. doi:10.1016/j.jmatprotec.2019.03.016
33. Ahmadi F, Simchi M, Perry JM, et al. Integrating machine learning and digital microfluidics for screening experimental conditions. *Lab Chip*. 2023;23(1):81-91.
34. Serdeczny MP, Comminal R, Pedersen DB, Spangenberg J. Experimental validation of a numerical model for the strand shape in material extrusion additive manufacturing. *Addit Manuf*. 2018;24:145-153. doi:10.1016/j.addma.2018.09.022
35. Kazmer DO, Colon AR, Peterson AM, Kim SK. Concurrent characterization of compressibility and viscosity in extrusion-based additive manufacturing of acrylonitrile butadiene styrene with fault diagnoses. *Addit Manuf*. 2021;46:102106. doi:10.1016/j.addma.2021.102106
36. Abbott AC, Tandon GP, Bradford RL, Koerner H, Baur JW. Process-structure-property effects on ABS bond strength in fused filament fabrication. *Addit Manuf*. 2018;19:29-38. doi:10.1016/j.addma.2017.11.002
37. Coogan TJ, Kazmer DO. Bond and part strength in fused deposition modeling. *Rapid Prototyp J*. 2017;23(2):414-422. doi:10.1108/RPJ-03-2016-0050
38. Ai JR, Peng F, Joo P, Vogt BD. Enhanced dimensional accuracy of material extrusion 3D-printed plastics through filament architecture. *ACS Appl Polym Mater*. 2021;3(5):2518-2528. doi:10.1021/acsapm.1c00110
39. Coogan TJ. In-line monitoring and prediction of viscosity, interlayer contact, and strength in the fused deposition modeling process. Doctoral Dissertation. 2019.
40. Levinskas L. Research of dimensional accuracy and surface quality dependency on printing speed of FDM 3D printed parts. Master's Thesis. 2019.
41. Stepashkin AA, Chukov DI, Senatov FS, Salimon AI, Korsunsky AM, Kaloshkin SD. 3D-printed PEEK-carbon fiber (CF) composites: structure and thermal properties. *Compos Sci Technol*. 2018;164:319-326. doi:10.1016/j.compscitech.2018.05.032
42. Choong GYH, Lew CY, de Focatiis DSA. Role of processing history on the mechanical and electrical behavior of melt-compounded polycarbonate-multiwalled carbon nanotube nanocomposites. *J Appl Polym Sci*. 2015;132(28):42277. doi:10.1002/app.42277
43. Bulanda K, Oleksy M, Oliwa R, et al. Polymer composites based on polycarbonate (PC) applied to additive manufacturing using melted and extruded manufacturing (MEM) technology. *Polymers (Basel)*. 2021;13(15):2455. doi:10.3390/polym13152455
44. Costa P, Dios JR, Cardoso J, et al. Polycarbonate based multifunctional self-sensing 2D and 3D printed structures for aeronautic applications. *Smart Mater Struct*. 2021;30(8):085032. doi:10.1088/1361-665X/ac0cbe
45. Tang Z, Okazaki S. All-atomistic molecular dynamics study of the glass transition of amorphous polymers. *Polymer (Guildf)*. 2022;254:125044. doi:10.1016/j.polymer.2022.125044
46. Kuznetsov VE, Solonin AN, Tavitov A, Urzhumtsev O, Vakulik A. Increasing strength of FFF three-dimensional printed parts by influencing on temperature-related parameters of the process. *Rapid Prototyp J*. 2020;26(1):107-121. doi:10.1108/RPJ-01-2019-0017
47. Braconnier DJ, Jensen RE, Peterson AM. Processing parameter correlations in material extrusion additive manufacturing. *Addit Manuf*. 2020;31:100924. doi:10.1016/j.addma.2019.100924
48. Rohde S, Cantrell J, Jerez A, et al. Experimental characterization of the shear properties of 3D–printed ABS and polycarbonate parts. *Exp Mech*. 2018;58(6):871-884. doi:10.1007/s11340-017-0343-6
49. Ai JR, Vogt BD. Size and print path effects on mechanical properties of material extrusion 3D printed plastics. *Prog Addit Manuf*. 2022;7(5):1009-1021. doi:10.1007/s40964-022-00275-w
50. Allum J, Moetazedian A, Gleadall A, Silberschmidt VV. Discussion on the microscale geometry as the dominant factor for strength anisotropy in material extrusion additive manufacturing. *Addit Manuf*. 2021;48:102390. doi:10.1016/j.addma.2021.102390


## SUPPORTING INFORMATION

Additional supporting information can be found online in the Supporting Information section at the end of this article.

**How to cite this article:** Adisa AO, Colon AR, Kazmer DO, Peterson AM. Interrelationships between process parameters, cross-sectional geometry, fracture behavior, and mechanical properties in material extrusion additive manufacturing. *Polym Eng Sci*. 2023;63(11): 3906-3918. doi:10.1002/pen.26495